

# Exploring the Physical Properties of the Cool Circumgalactic Medium with a Semi-Analytic Model

TING-WEN LAN<sup>1</sup> AND HOUJUN MO<sup>2,3</sup>

<sup>1</sup>*Kavli IPMU, the University of Tokyo (WPI), Kashiwa 277-8583, Japan*

<sup>2</sup>*Department of Astronomy, University of Massachusetts, LGRT-B619E, 710 North Pleasant Street, Amherst, MA, 01003, USA*

<sup>3</sup>*Physics Department and Center for Astrophysics, Tsinghua University, Beijing 10084, China*

## ABSTRACT

We develop a semi-analytic model to explore the physical properties of cool pressure-confined circumgalactic clouds with mass ranging from 10 to  $10^8 M_\odot$  in a hot diffuse halo. We consider physical effects that control the motion and mass loss of the clouds, and estimate the lifetime and the observed properties of individual cool gas clouds inferred from the CLOUDY simulation. Our results show that the cool pressure-confined gas clouds have physical properties consistent with absorption line systems with neutral hydrogen column densities  $N_{\text{HI}} \geq 10^{18.5} \text{ cm}^{-2}$  such as strong metal absorbers, sub-DLAs, and DLAs. The cool circumgalactic clouds are transient due to evaporation and recycling and therefore a constant replenishment is needed to maintain the cool CGM. We further model the ensemble properties of the cool CGM with clouds originated from outflows, inflows, or/and in-situ formation with a range of initial cloud mass function and velocity distribution. We find that only with a certain combination of parameters, an outflow model can broadly reproduce three cool gas properties around star-forming galaxies simultaneously: the spatial distribution, down-the-barrel outflow absorption, and gas velocity dispersion. Both a constant insitu model and gas inflow model can reproduce the observed covering fractions of high  $N_{\text{HI}}$  gas around passive galaxies but they fail to reproduce sufficient number of low  $N_{\text{HI}}$  systems. The limitations and the failures of the current models are discussed. Our results illustrate that semi-analytic modeling is a promising tool to understand the physics of the cool CGM which is usually unresolved by state-of-the-art cosmological hydrodynamic simulations.

*Keywords:* quasars: absorption lines, galaxies: halos, intergalactic medium

## 1. INTRODUCTION

Gas around galaxies, the circumgalactic medium (CGM, Tumlinson et al. 2017, for a review), plays a key role in galaxy formation and evolution. As the interface between galaxies and the intergalactic medium (IGM), the CGM contains signatures of gas flow processes that drive the evolution of galaxies. Since the first discovery of the CGM (Bergeron 1986), studies have revealed the complex nature of the CGM. The CGM is multi-phase, consisting of gas with wide ranges of temperature and density. In addition, the properties of galaxies and their CGM have complicated relationships; while cool gas ( $\sim 10^4$  K) appears to exist around both star-forming and passive galaxies (e.g., Chen et al. 2010; Thom et al. 2012; Lan et al. 2014), warm gas is much more abundant around star-forming galaxies than around passive galaxies (e.g., Tumlinson et al. 2011).

To interpret these observational results, simulations and theories for the CGM have been developed. Recently, many studies have attempted to address the origin of the excess of warm gas traced by OVI absorption lines (diffuse gas with  $\sim 10^{5.5}$  K assuming collisional ionization) around star-forming galaxies (e.g., Bordoloi et al. 2017; Faerman et al. 2017; Mathews & Prochaska

2017; Nelson et al. 2018; McQuinn & Werk 2018; Stern et al. 2018). On the other hand, although cool gas has been observed ubiquitously around galaxies (as, e.g., traced by MgII absorption lines), only limited attempts have been made to model and understand the origin of the cool halo gas (e.g., Mo & Miralda-Escude 1996; Maller & Bullock 2004; Kaufmann et al. 2009; Bordoloi et al. 2014; Faucher-Giguère et al. 2016; van de Voort et al. 2018). More importantly, observations (e.g., Rauch et al. 1999; Rigby et al. 2002; Prochaska & Hennawi 2009; Lan & Fukugita 2017) and simulations (e.g., McCourt et al. 2018; Liang & Remming 2018; Sparre et al. 2018; Suresh et al. 2018) have shown that the physical scale relevant to the cool circumgalactic gas is of the order of a few tens of parsec or even smaller, which is several orders of magnitude smaller than the resolution of any current galaxy hydrodynamic simulations (see Figure 9 in Sparre et al. 2018). This discrepancy poses a challenge to understanding the physics for the CGM and galaxy formation.

To overcome the limitation of numerical resolution, we develop a semi-analytic model for the cool circumgalactic gas, motivated by earlier analytic works. We revisit the idea of cool gas clouds being in pressure equilibrium with an ambient hot halo gas (Mo & Miralda-Escude

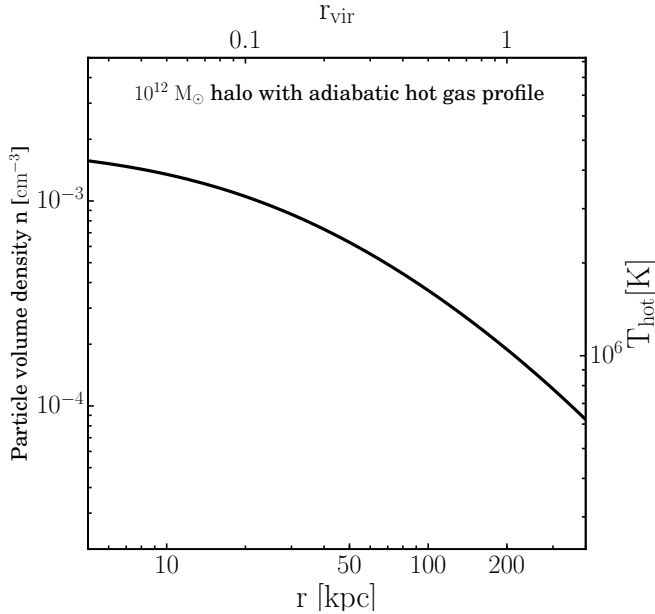


**Figure 1.** Hot gas density and temperature profiles.

1996; Maller & Bullock 2004) and estimate their lifetime, motion, and trajectory by taking into account the effects of gravity, ram pressure and heat evaporation. We model the ensemble properties of the cool gas clouds in halos considering scenarios of outflows, inflows, and in-situ formation. With this flexible model, our goal is to explore how physical mechanisms affect the properties of the CGM and to constrain parameter space of these mechanisms with observations.

This paper is organized as follows. In Section 2, we describe the considered physical effects for cool gas clouds. In Section 3, we summarize the evolution of individual clouds and present the ensemble properties of cool gas and their evolution. We discuss other implications in Section 4 and summarize our results in Section 5. Throughout the paper we adopt a flat  $\Lambda$ CDM cosmology with  $h = 0.7$  and  $\Omega_M = 0.3$ .

## 2. MODEL SETUP

To explore the properties of cool pressure-confined clouds in the CGM, we first introduce the model components that control the motion and the lifetime of individual clouds (§2.1). We then describe our outflow and inflow models to populate an ensemble of clouds into the CGM and to characterize the statistical properties of the cool clouds (§2.2).

### 2.1. Model components for individual clouds

**Basic properties-** The evolution of cool clouds is modeled under the influence of a dark matter halo and a hot diffuse gas halo. We adopt a  $10^{12} M_\odot$  dark matter halo, which corresponds to  $\sim L^*$  galaxies (Yang et al. 2003, 2012), with a NFW profile (Navarro et al. 1996) and concentration  $c = 10$ . This halo mass is chosen

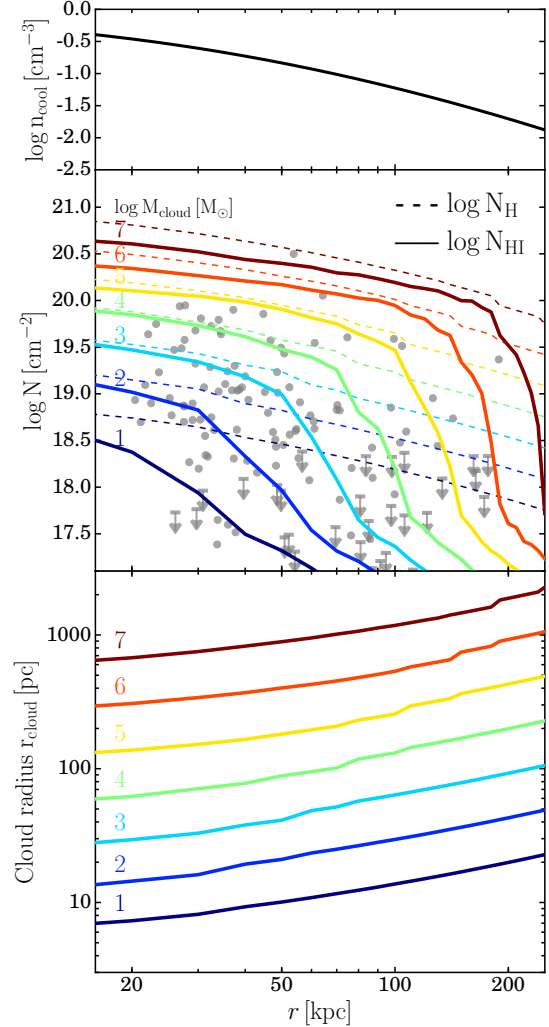


**Figure 2.** Cloud properties as a function of position. *Top:*  $10^4$  K cool gas volume density. *Middle:* neutral hydrogen (solid color lines) and total hydrogen (dashed color lines) column densities as a function of cloud mass. The data points show the neutral hydrogen column densities traced by strong MgII absorbers from observations. Arrows indicate upper limits. Note that data points are in the projected distance. *Bottom:* cloud radius as a function of mass.

in order to compare with available observational measurements. The effect of halo mass will be discussed in Section 4. For the hot gaseous halo, we use the gas profile derived by Maller & Bullock (2004), assuming that the initial hot gas had cooled over 6 billion years and the residual hot gas had reached hydrostatic equilibrium adiabatically at  $z = 0.5$ . The metallicity of the hot gas is assumed to be 0.1 solar. Figure 1 shows the adopted hot gas density (left axis) and the temperature (right axis) profiles. This hot gas profile is similar to the

observed hot gas profile of the Milky Way (e.g., [Gupta et al. 2017](#)).

The physical properties of cool gas clouds are obtained by assuming that *cool gas clouds are in pressure equilibrium with the surrounding hot gas halo* (e.g. [Mo & Miralda-Escude 1996](#)),

$$n_{\text{cloud}} T_{\text{cloud}} = n_{\text{hot}} T_{\text{hot}}. \quad (1)$$

This is motivated by the fact that a gas cloud can establish pressure equilibrium with its surrounding typically within the sound crossing time. For a cloud with  $10^4 M_{\odot}$ ,  $n \sim 0.3 \text{ cm}^{-3}$ , and  $T \sim 10^4 \text{ K}$ , the sound crossing time is about 10 Myr, much shorter than the survival time of the clouds, which is greater than 100 Myr. We assume that the temperature of gas clouds is  $10^4 \text{ K}$  with spherical geometry. The physical properties of a cool gas cloud of a given mass  $M_{\text{cloud}}$ , such as its size  $r_{\text{cloud}}$ , volume density  $n_{\text{cloud}}$ , the total hydrogen column density  $N_{\text{H}}$ , neutral hydrogen column density  $N_{\text{HI}}$ , and ionization fraction, are then obtained self-consistently by using CLOUDY simulation ([Ferland et al. 2013](#)). Gas clouds are assumed to be photo-ionized by an extra-galactic radiation field described by the model of [Haardt & Madau \(2001\)](#)<sup>1</sup>.

In Figure 2, we show the properties of cool clouds as functions of cloud mass and location in the halo. The top panel shows the volume densities of the cool gas clouds. In the middle panel, the solid color lines show the neutral hydrogen column densities  $N_{\text{HI}}$  of clouds and the dashed lines show the total hydrogen column densities. The neutral hydrogen column densities fall within the range between  $10^{18}$  and  $10^{20.5} \text{ cm}^{-2}$ , similar to that observed in sub-damped Lyman systems (strong Lyman-limited systems) and damped Lyman systems. For comparison, the grey squares show the neutral hydrogen column densities traced by strong MgII absorbers, obtained by using MgII galaxy-absorber pairs from [Nielsen et al. \(2013\)](#) and the empirical relationship between MgII rest equivalent width and neutral hydrogen column density from [Lan & Fukugita \(2017\)](#):

$$N_{\text{HI}} \simeq 10^{19} \left( \frac{W_{\lambda 2796}}{1 \text{ \AA}} \right)^{1.7} (1+z)^{1.9} \text{ cm}^{-2}. \quad (2)$$

Note, however, that the grey data points use the projected distance instead of the three-dimensional distance in the halo.

At small scales, the neutral hydrogen column density depends on the volume density of clouds:

$$N_{\text{HI}} \propto n_{\text{HI}} \times r_{\text{cloud}} \propto n_{\text{H}}^{2/3} M_{\text{cloud}}^{1/3}. \quad (3)$$

However, beyond a certain distance scale, the neutral hydrogen column densities drop rapidly due to that the

volume density of the cloud is too low to be self-shielded from the ionization radiation field. This scale depends on the cloud mass, as shown in the figure. In the bottom panel of Figure 2, we show cloud radius (assuming spherical shape) as a function of mass and distance. The cloud radius ranges from 10 pc to a few hundred pc, with a typical value of  $\sim 100 \text{ pc}$  for cloud mass  $\sim 10^4 M_{\odot}$ .

**Motion and survival-** To model the motion and survival of the cool clouds in the halo, we consider the following effects:

- **Motions of clouds -**

the motion of a cloud is governed by the gravitational potential provided by the dark matter halo and the ram pressure of the hot gas halo:

$$M_{\text{cloud}} \frac{d^2 r}{dt^2} = - \frac{GM_{\text{DM}}(< r) M_{\text{cloud}}}{r^2} - F_{\text{ram}} \quad (4)$$

where  $G$  is the gravitational constant. The ram pressure drag force from the hot gas (e.g., [Maller & Bullock 2004](#)), which always decelerates the cloud, is defined as

$$F_{\text{ram}} = \frac{1}{2} C_d \rho_{\text{hot}}(r) v_{\text{cloud}}(r)^2 \times \pi r_{\text{cloud}}^2 \quad (5)$$

where  $\rho_{\text{hot}}(r)$  is the mass density of hot gas at position  $r$ ,  $v_{\text{cloud}}(r)$  is the radial velocity of the cloud, and  $r_{\text{cloud}}$  is the radius of the cloud. Following [Maller & Bullock \(2004\)](#), we set ram pressure efficiency,  $C_d$ , to be 1 as the default value but will explore the effect of changing its value in Section 3.3.1. The cloud deceleration from ram pressure scales with the column density of clouds as  $N_{\text{H}}^{-1}$ . Thus, the ram pressure effect is smaller for more massive clouds. In this paper, we only consider radial motion of clouds.

- **Cloud disruptions -** there are several mechanisms that could affect the mass of a cloud. [Mo & Miralda-Escude \(1996\)](#) (see also [Maller & Bullock \(2004\)](#)) provides a detail summary about the possible mechanisms. Here we briefly discuss the key mechanisms:

**(1) Self-gravity -** The upper limit of a cloud mass in our analysis is constrained by the Jeans mass ([Jeans 1902](#)) above which the cloud collapses due to its self-gravity. The Jeans mass of clouds in our model setup is about  $10^8 M_{\odot}$ .

**(2) Hydrodynamic instability -** When a dense cloud moves through a hot gas halo, the cloud is subject to the hydrodynamic instability, such as Kelvin-Helmholtz instability and Rayleigh-Taylor instability. The characteristic timescale of the instabilities (e.g. [Murray et al. 1993](#)) are

$$t_{\text{instability}} \sim \frac{r_{\text{cloud}}}{V_{\text{cloud}}} \sqrt{\frac{T_{\text{Hot}}}{T_{\text{cloud}}}}. \quad (6)$$

<sup>1</sup> We use the unpublished updated 2005 version implemented in the CLOUDY simulation.

Based on the characteristic timescale, a cool gas cloud can only travel a distance that is about 10 times its radius (assuming  $T_{\text{Hot}} \sim 100 T_{\text{cloud}}$ ) before it is destroyed by the instability. However, several studies have shown that other mechanisms can suppress the effects of hydrodynamical instabilities, such as radiative cooling (Vietri et al. 1997), magnetic fields (e.g. McCourt et al. 2015), and the presence of heat conduction layers (Armillotta et al. 2017), and mixing layer between cool and hot gas (Gronke & Oh 2018). Motivated by these studies, we assume that the clouds are intact under the effect of the hydrodynamic instability.

**(3) Heat evaporation** - Surrounded by hot ambient gas, cool gas clouds are subject to mass loss due to the heating by the hot gas. The classic mass loss rate due to the evaporation is derived by Cowie & McKee (1977):

$$\begin{aligned} \dot{M}_{\text{cloud,classic}} &= \frac{dM_{\text{cloud}}}{dt} \\ &= 2.75 \times 10^4 T_{\text{hot}}^{5/2} r_{\text{cloud}} \left( \frac{30}{\ln \Lambda} \right) \text{g s}^{-1} \\ &= 0.44 \left( \frac{T}{10^6 \text{ K}} \right)^{5/2} \left( \frac{r_{\text{cloud}}}{\text{pc}} \right) \frac{M_{\odot}}{\text{Myr}}, \end{aligned} \quad (7)$$

where  $\ln \Lambda$  is the Coulomb logarithm with value about 30. Dalton & Balbus (1993) generalize the mass loss rate including the case when the heat conduction is saturated:

$$\dot{M}_{\text{cloud}} = f w \dot{M}_{\text{cloud,classic}}, \quad (8)$$

where  $w$  is the modified factor depending on the saturation parameter,

$$\sigma_0 = \frac{2\kappa_{\text{hot}} T_{\text{hot}}}{25\Phi \rho_{\text{hot}} c_{\text{hot}}^3 r_{\text{cloud}}} \quad (9)$$

with  $\kappa_{\text{hot}} = 1.84 \times 10^{-5} T_{\text{hot}}^{5/2} (\ln \Lambda)^{-1}$  [cgs],  $\Phi$  being an efficiency factor of the order of unity, which is set to be 1, and  $c_{\text{hot}}$  being the sound speed of the hot gas. If  $\sigma_0$  is greater than 1, the saturation will reduce the mass loss rate to  $w \dot{M}_{\text{cloud,classic}}$ . If  $0.027 < \sigma_0 < 1$ , the cloud undergoes classical evaporation. Finally, we introduce a suppression factor  $f$  for the evaporation rate in Eq. 7. We adopt  $f = 0.05$  to account for the effect of other mechanisms such as magnetic field (e.g., Chandran & Cowley 1998) on the efficient of mass evaporation. We note that some studies have constrained the  $f$  value to be about 0.01 or lower (e.g., Binney & Cowie 1981; Nipoti & Binney 2004). We discuss the effect of  $f$  value in Section 4.

## 2.2. Model components for an ensemble of clouds

To investigate how the statistical properties of cool clouds, such as their spatial distribution, depend on the origin of the clouds, we populate an ensemble of clouds in a halo by considering the following model components:

- **Origins of cool gas clouds** - we consider cool gas clouds have three origins: (1) outflow gas clouds ejected at 1 kpc from the center of the halo, (2) inflow gas from the virial radius of the halo, and (3) in-situ gas formed in the halo with distribution following NFW and power law profiles.
- **Gas flow mass rate** - we consider a burst gas flow and a constant gas flow for the outflow models. Mass outflow rate for the burst model follows an exponential form similar to the star-formation history of galaxies (e.g. Bruzual & Charlot 2003):

$$\frac{dM_{\text{outflow}}}{dt} = 340 e^{-t/200\text{Myr}} M_{\odot}/\text{yr}. \quad (10)$$

For the constant outflow and inflow models, we assume a constant gas flow with  $20 M_{\odot} \text{ yr}^{-1}$ . These models eject  $8 \times 10^{10} M_{\odot}$  in total over 4000 Myr, and the value is chosen to produce the cool CGM mass of about  $10^{10} M_{\odot}$ , similar to that observed. We note that there is a degeneracy between the gas flow rate and the evaporation suppression factor  $f$  for the evaporation, as discussed in Section 4.

- **Initial cloud mass function** - to populate the total gas mass into clouds, we introduce an initial cloud mass function to account for possibly coverage of cloud masses. We assume that (i) the mass spectrum of cool gas clouds follows a power law distribution with a power  $\alpha$ :

$$N(M_{\text{cloud}}) \propto M_{\text{cloud}}^{\alpha}, \quad (11)$$

(ii) the mass spectrum follows a Schechter function with a power  $\alpha$  and a characteristic cloud mass  $M_*$ :

$$N(M_{\text{cloud}}) \propto M_{\text{cloud}}^{\alpha} \times e^{-M_{\text{cloud}}/M_*}. \quad (12)$$

In addition, we put limits on the initial maximum and minimum cloud masses. The maximum cloud mass is  $10^8 M_{\odot}$  above which the clouds collapse due to self-gravity. The minimum cloud is set to be  $10^2 M_{\odot}$ . The initial cloud mass function plays an important role in the structure of the circumgalactic medium. The value of  $\alpha$  determines how the total cloud mass is distributed in cloud mass and, therefore, the column density  $N_{\text{HI}}$  distribution in the CGM and the covering fraction of gas clouds around galaxies. We will pay special attention to how the properties of the CGM depend on  $\alpha$ .

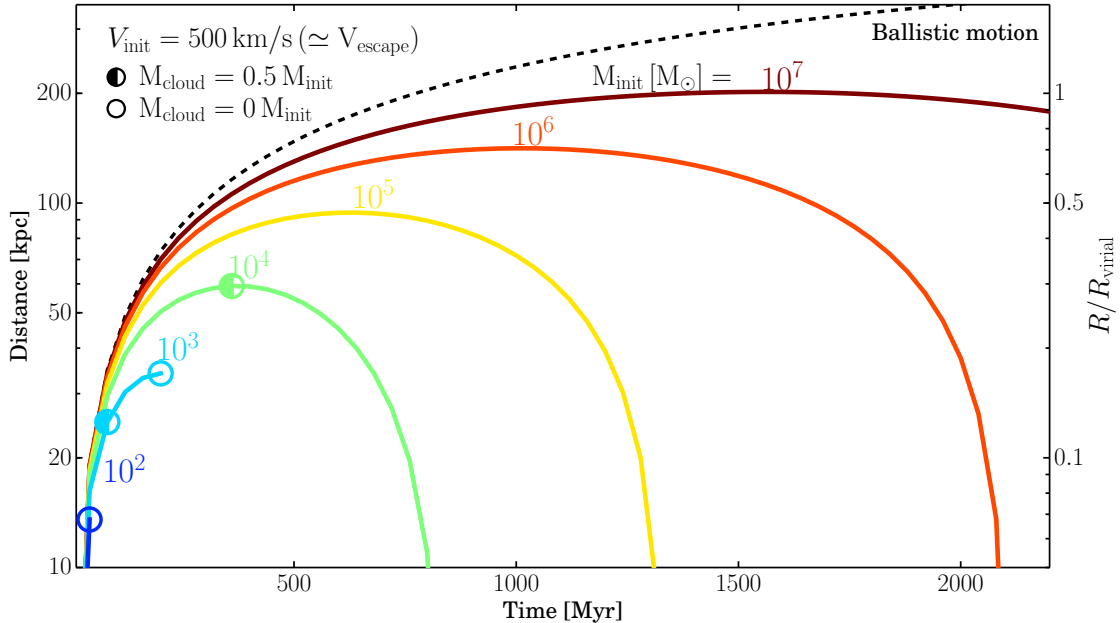


**Figure 3.** Examples of trajectories of clouds with initial velocity of 500 km/s (escaping velocity) and initial mass from  $10^2$  to  $10^7 M_\odot$ . Half fill cycles (empty cycles) indicate the times when clouds loss half (all) of their initial mass due to evaporation. The dashed line shows the trajectory without the effect of hot gas. The hot gas prevents the escape of clouds with ram pressure and destroys the small cool clouds with evaporation.

- **Velocity distribution** - we assume that the velocity distribution of outflow clouds follows a normal distribution with mean velocity equal to 300, 500, or 700 km/s, and a width of 200 km/s. These numbers are motivated by observations (e.g. Rubin et al. 2014) and theoretical models (e.g. Murray et al. 2011). Clouds are assumed to be ejected from the center isotropically.

### 3. RESULTS

#### 3.1. Evolution of individual clouds

We first study the motion and mass evolution of clouds derived from Equations (4) and (8). Figure 3 shows examples of the trajectories of clouds with masses from  $10^2$  (blue line) to  $10^7 M_\odot$  (red line), and with initial velocity  $V_{\text{init}} = 500$  km/s ejected at 1 kpc from the center of the halo. Ballistic motion without the effect of ram pressure is shown with the black dashed line. The half-filled and open circles indicate the times when the cloud has lost half of its initial mass and is totally evaporated, respectively. As shown in the figure, the effect of ram pressure depends on the mass of clouds: massive clouds are able to travel beyond 100 kpc while small clouds are stopped by ram pressure and fall back within 50 kpc. Without ram pressure, clouds with the same initial velocity should all follow the ballistic motion. For cloud masses  $< 10^7 M_\odot$ , no clouds can escape the halo even if the initial velocity is comparable to the escape velocity of the gravitational potential. In addition to ram pressure, the hot ambient gas can also remove gas

from clouds via heat evaporation. Clouds with masses less than  $10^4 M_\odot$  lose all the mass within a few hundred Myr due to evaporation, while clouds with masses greater than  $10^4 M_\odot$  fall back to the center with a fraction of their initial masses. The estimated evaporation timescales for clouds are similar to the timescale estimation from hydrodynamical simulations by Armillotta et al. (2017) for individual clouds.

We summarize the fates of clouds with various initial velocities and masses ejected at 1 kpc from the halo center in Figure 4. The left panel shows the maximum distance that a cloud can travel and the right panel shows the survival time of the clouds. The fates of clouds can be classified into three categories:

1. **Evaporation (left):** Clouds with relative low masses and high velocities lose all their masses due to evaporation within 50-1000 Myr while traveling in the halo. Even with extreme initial velocities, small clouds can only reach about 50-100 kpc from the center before being evaporated.
2. **Survival (top right):** Clouds with high masses and high velocities can survive over 4 Gyr and most of them can escape the halo.
3. **Recycling (bottom right):** Clouds with high masses but low velocities eventually fall back to the halo center with a fraction of their initial masses. The timescale for clouds to be recycled is about 500-1000 Myr depending on the initial ve-



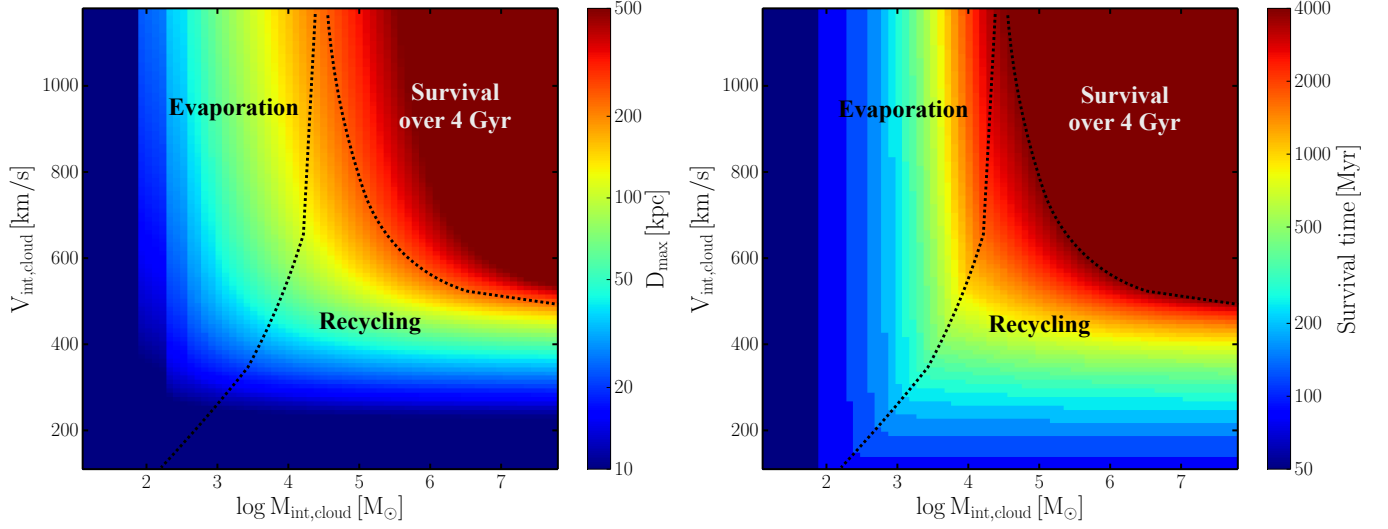


**Figure 4.** Summary of the fates of outflowing clouds with various initial masses and velocities. *Left:* maximum distance. *Right:* survival time.

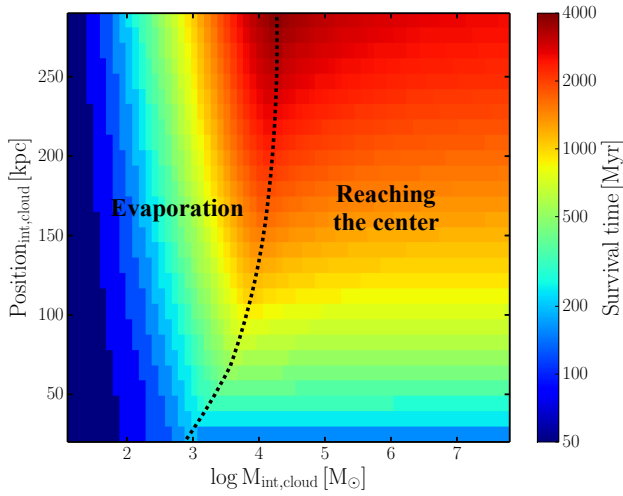


**Figure 5.** Summary of the fates and survival time of inflow clouds with various initial masses and positions.

locity consistent with results from hydrodynamical simulations (e.g., Ford et al. 2014; Anglés-Alcázar et al. 2017).

In addition to clouds ejected from the halo center, we also model the gas clouds falling from a given initial position towards the halo center with no initial velocity. The fates of the inflowing gas clouds are summarized in Figure 5 showing the survival time of the clouds. Similarly to the outflow case, clouds with low masses are evaporated in the circumgalactic space while massive clouds can reach the halo center with a fraction of their initial

masses. For clouds falling from the halo virial radius ( $\sim 200$  kpc), it takes about 2 Gyr to reach the center.

### 3.2. Mass Evolution

With the properties and fates of individual clouds modeled, we now explore how the ensemble of clouds evolves with time. To do so, we eject clouds with a given flow rate and a given initial cloud mass function, as discussed in Section 2.2. We estimate the fractions of initial ejected mass (1) staying in the circumgalactic space, (2) moving beyond the virial radius, (3) evaporated, and (4) falling back into the center, and explore how the different fractions change with model parameters. Figure 6 shows the results for three modes of gas flow models: the burst outflow model (left column), constant outflow (middle column), and constant inflow models (right column). We also explore three initial mass functions, power laws with  $\alpha = 0$  (top panel) and  $\alpha = -1$  (middle panel), and a Schechter function with  $\alpha = -1$  and  $M_* = 10^{5.5} M_{\odot}$  (bottom panel). The color lines indicate masses in different components. Mass within and outside the virial radius are shown with the blue and purple lines, respectively. The green line indicates the recycled mass that falls back to the center, and the red line shows the amount of mass that is evaporated. The black dashed line shows the total ejected mass. The gas flow rate is selected to eject  $8 \times 10^{10} M_{\odot}$  over 4 Gyr. The mean initial velocity for the outflow models is 500 km/s.

Let us first focus on the burst outflow model with  $\alpha = 0$ , shown in top-left panel, in which all the mass ( $8 \times 10^{10} M_{\odot}$ ) is ejected in 500 Myr. The mass in the circumgalactic medium reaches its maximum at around 400 Myr, and declines afterwards. After 1 Gyr,  $\sim 40\%$  of the total mass has moved beyond the virial radius

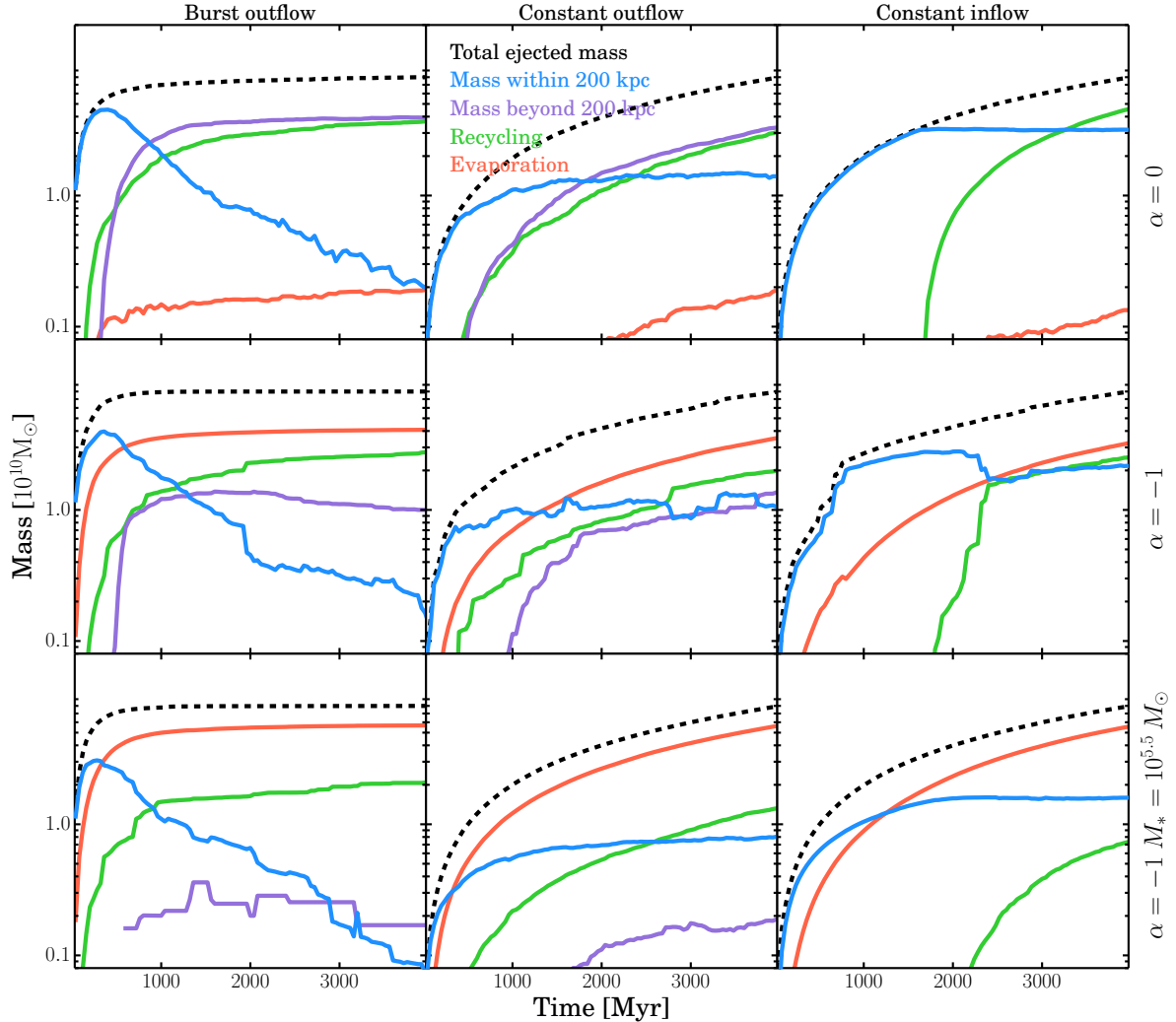


**Figure 6.** Mass evolution of ejected clouds with three gas flow modes. *Left:* Burst outflow models; *Middle:* constant outflow models; *Right:* constant inflow models. The total ejected mass is shown with the black lines. The masses in the circumgalactic space and moving beyond the virial radius are shown in blue and purple, respectively. The mass that recycles back to the center is shown in green and that gets evaporated is shown in red.

and a similar fraction of the mass recycled back to the center. Only a small fraction of mass remains in the halo (15%) or gets evaporated (5%). This demonstrates that a single burst event cannot sustain the circumgalactic medium for a timescale of billion years. In contrast, in the constant outflow model, shown in the top middle panel, the mass in the circumgalactic region can reach  $\sim 10^{10} M_{\odot}$  and remains more or less constant. This is due to the balance between the constant mass outflow, the recycled mass, and the escaped mass. As in the burst outflow,  $\sim 40\%$  of the ejected mass returns to the center as recycled mass, while  $\sim 40\%$  escapes the halo. The mass evolution of the constant inflow model behaves similarly to the constant outflow model except that it takes about 2000 Myr for the inflowing clouds to reach the halo center.

This mass evolution also depends on the shape of the initial mass function: the typical cloud mass decreases and the evaporation timescale becomes shorter as  $\alpha$  decreases. By changing the shape of the initial mass function from  $\alpha = 0$  to  $\alpha = -1$ , the amount of evaporated mass increases by a factor of 10, as shown in the middle panels of Figure 6. Finally, adopting a Schechter function with  $\alpha = -1$  and  $M_* = 10^{5.5} M_{\odot}$  as the initial cloud mass function further reduces the number of massive clouds and enhances the mass fraction of evaporation to about 80%, as shown in the bottom panels of Figure 6. One interesting implication is that heat evaporation reduces the total cloud mass from outflows. Therefore, the outflow mass estimated from the cool CGM mass is only a lower limit (e.g., Lan & Mo 2018) and it can be an order of magnitude lower than the intrinsic outflow

mass depending on the shape of the mass function. Similarly, the evaporation reduces the total infalling cloud mass that reaches the center. This might be a possible mechanism to prevent further star-formation in passive galaxies (see also Zahedy et al. 2018). These results demonstrate that the total mass in the CGM depends on the shape of the initial cloud mass function. In the following, we will show that the shape of the initial mass function also plays an important role in determining the profile of the circumgalactic medium.

### 3.3. Spatial distribution of cool gas clouds

We now investigate the spatial distribution of the pressure-confined gas clouds as a function of different initial mass function and initial velocity. To guide the exploration, we compare our modeled gas properties with the observed neutral hydrogen gas around star-forming and passive galaxies at redshift 0.5. To this end, we use the distribution of the neutral hydrogen traced by strong MgII absorbers. Such absorbers, with  $W_{2796} > 0.4 \text{ \AA}$ , have been considered as a tracer of the cool circumgalactic gas with neutral hydrogen column densities  $N_{\text{HI}} > 10^{18.5} \text{ cm}^{-2}$  and volume densities  $n_{\text{H}} \sim 0.3 \text{ cm}^{-3}$  (e.g., Rao et al. 2006; Ménard & Chelouche 2009; Lan & Fukugita 2017), consistent with the properties of the pressure-confined cool clouds in our model. Strong MgII absorbers have been observed around both star-forming and passive galaxies, and their distributions around both types of galaxies are similar on large scales ( $r_p > 50 \text{ kpc}$ ) (e.g., Chen et al. 2010; Nielsen et al. 2013; Lan et al. 2014; Lan & Mo 2018). Within 50 kpc, however, there is more MgII absorption around star-forming galaxies than around passive galaxies. This excess absorption is most likely associated with outflows, as is inferred from the azimuthal angle distribution (e.g., Bordoloi et al. 2011; Kacprzak et al. 2012; Lan & Mo 2018). In our analysis, we use the MgII covering fraction at redshift 0.5 around galaxies with stellar mass  $\sim 10^{10.8} M_{\odot}$  provided by Lan et al. (2014) with  $0.4 < W_{\lambda 2796} < 0.8 \text{ \AA}$ ,  $0.8 < W_{\lambda 2796} < 1.5 \text{ \AA}$ , and  $W_{\lambda 2796} > 1.5 \text{ \AA}$ , as the proxy of neutral hydrogen covering fraction with  $18.6 < \log N_{\text{HI}}/\text{cm}^{-2} < 19.1$ ,  $19.1 < \log N_{\text{HI}}/\text{cm}^{-2} < 19.6$ , and  $\log N_{\text{HI}}/\text{cm}^{-2} > 19.6$ , respectively, based on Equation (2).

Our goal is to explore how different physical mechanisms affect the gas properties by using observational measurements as a guidance. To this end, we will examine the effects of individual model parameters one by one.

#### 3.3.1. Constant outflow models

In this subsection, we explore how the ensemble properties of cool gas clouds depend on the initial cloud mass function and the initial cloud velocity by using constant outflow models as examples.

**The effects of initial cloud mass function** are illustrated in Figure 7, which shows the structure of the

circumgalactic medium as a function of the shape of the initial cloud mass function. Here the mean initial cloud velocity is set to be 500 km/s and a constant outflow rate of  $20 M_{\odot}/\text{yr}$  is assumed. Results are shown for the snapshot at 2 Gyr. We show only 10% of total number of clouds with sizes of data points reflecting 3 times of the physical sizes of clouds. The total mass in the cool circumgalactic medium is about  $10^{9.5} - 10^{10} M_{\odot}$ , with the exact value depending on the shape of the initial mass function. The color indicates the  $N_{\text{HI}}$  the gas cloud.

The morphology and structure of the cool CGM both depend on the initial cloud mass function. For a power law function with  $\alpha = 0$ , the CGM consists of thousands of massive clouds with  $N_{\text{HI}} > 10^{20} \text{ cm}^{-2}$  (left panel), while the CGM produced by a power law mass function with  $\alpha = -1$  contains millions of gas clouds with  $N_{\text{HI}}$  ranging from  $10^{18.5}$  to  $10^{20.5} \text{ cm}^{-2}$  (middle panel). With an exponential cutoff in the massive end, the Schechter initial mass function further reduces the number of massive clouds (red dots) and produces even more small clouds (right panel).

To quantify the effects of the initial cloud mass function, we estimate the covering fraction of gas clouds as a function of  $N_{\text{HI}}$  and compare the results with the observed ones in the top panel of Figure 8. The predicted covering fractions are estimated from the interceptions with clouds out of 50,000 random sightlines with impact parameters  $\leq 250 \text{ kpc}$ . When multiple clouds are intercepted by a single sightline, the  $N_{\text{HI}}$  is the sum of the  $N_{\text{HI}}$  of individual intercepted clouds. The average neutral hydrogen gas covering fraction over the time interval between 2000 Myr and 4000 Myr produced by the power law mass functions with  $\alpha = 0$  and  $\alpha = -1$  are shown in purple and orange, respectively, with the bands showing the fluctuation of the covering fraction over time. With  $\alpha = 0$ , the gas covering fraction of  $N_{\text{HI}} < 10^{19.6} \text{ cm}^{-2}$  clouds is close to zero as almost all the outflow mass is carried by massive clouds, inconsistent with the observed covering fraction shown by the blue data points. On the other hand, the number of massive clouds is reduced and that of small clouds enhanced in the  $\alpha = -1$  model, and the predicted covering fraction of  $N_{\text{HI}} < 10^{19.6} \text{ cm}^{-2}$  is now of the same order as the observed one.

Finally, the results assuming a Schechter function with  $\alpha = -1$  and  $M_* = 10^{5.5} M_{\odot}$  for the cloud mass function are shown in green color. The Schechter function redistributes the mass in massive clouds ( $M_{\text{cloud}} > M_*$ ) into smaller ones, thereby further enhancing the gas covering fraction of systems with  $10^{18.6} < N_{\text{HI}} < 10^{19.6} \text{ cm}^{-2}$ . The difference between the orange (power law) and green lines (Schechter function) illustrates the effect of the mass function. Such an effect can also be seen from the spatial distribution shown in Figure 7. These results demonstrate that the initial cloud function can affect the structure the gas distribution around galaxies significantly, and so can be constrained by the observed



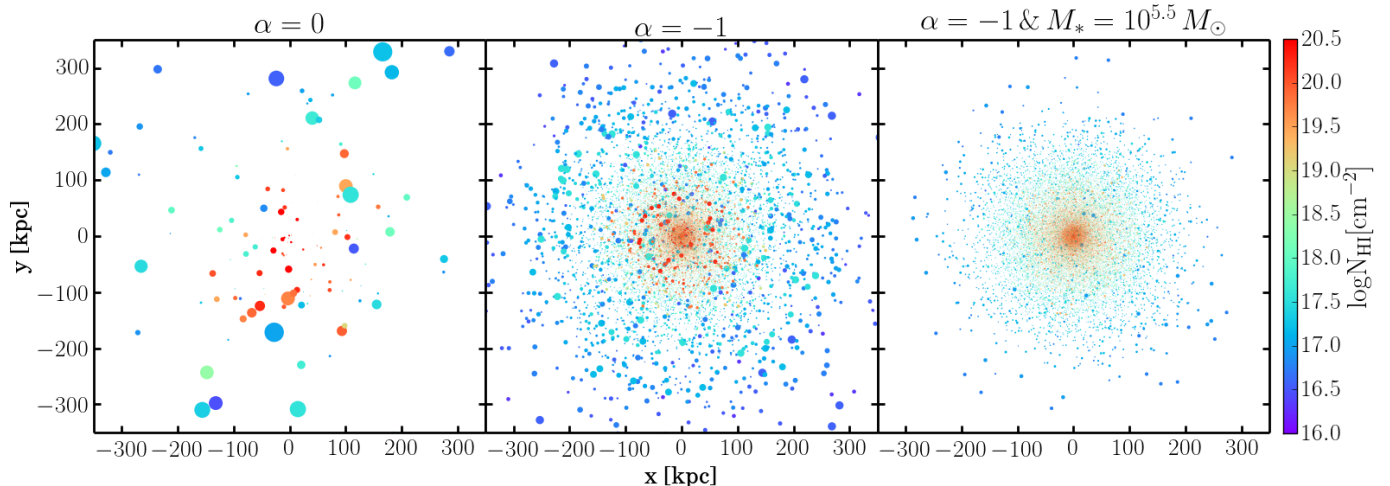


**Figure 7.** Snapshots of the spatial distribution of gas clouds in the constant outflow models with three different initial cloud mass functions at 2 Gyr. *Left:* a power law initial mass function with  $\alpha = 0$ . *Middle:* a power law initial mass function with  $\alpha = -1$ . *Right:* a Schechter-like initial mass function with  $\alpha = -1$  and  $M_* = 10^{5.5} M_\odot$ . Only 10% of the clouds are plotted with sizes reflecting 3 times of the physical sizes of the clouds. The color indicates its  $N_{\text{HI}}$ . The mean initial velocity is 500 km/s.

spatial gas distribution as a function of column densities. As one can see, the outflow model with the Schechter cloud mass function can reproduce roughly the observed gas covering fraction as a function of neutral hydrogen column densities.

**The effects of initial outflow velocity** are shown in the middle row of Figure 8, where results obtained from three initial outflow mean velocities, 300 (cyan dotted), 500 (green solid) and 700 (blue dashed lines) km/s are plotted. Comparing to the model with 500 km/s, the model with 300 km/s is insufficient for the clouds to propagate far enough. On the other hand, increasing the mean velocity to be 700 km/s will allow more clouds to propagate to larger distances. However, since the value of  $N_{\text{HI}}$  for a fixed cloud mass decreases rapidly at large distance, as shown in Fig. 2, the clouds that propagate to large distances do not contribute significantly to the covering fraction of the relatively high- $N_{\text{HI}}$  systems concerned here.

The initial outflow velocity in a galaxy may be constrained by the gas absorption observed toward the galaxy, i.e. through the so-called down-the-barrel observation. To do this, we assume that the effective radius of a galaxy is 5 kpc and calculate the absorption profile based on

$$\frac{I}{I_0}(v) = 1 - f_c(v) \times (1 - e^{-\tau}), \quad (13)$$

where  $I$  and  $I_0$  are the observed flux and the continuum, respectively,  $f_c(v)$  is the covering fraction of clouds at a given velocity, and  $\tau$  is the optical depth (e.g. Jones et al. 2018). Here we consider the optical thick region where absorption lines are saturated and  $\tau$  is large. In this case the above equation can be approximated as

$1 - f_c(v)$ . The left panel of Figure 9 shows our modeled down-the-barrel absorption. The cyan dotted, green solid, and blue dashed lines show the results with initial outflow velocity equal to 300, 500, and 700 km/s, respectively. For comparison, we also show the observed down-the-barrel strong MgII absorption of star-forming galaxies (blue histogram) from Zhu et al. (2015). We note that the observed profile includes not only the absorption from outflowing gas but also from interstellar gas, while the modeled profile includes only outflowing gas. As the interstellar gas absorption is expected to occur mostly around zero velocity, the observed blue-shifted absorption wing ( $< -200$  km/s) is expected to be due to outflowing gas, and so can be directly compared with the modeled profile. The models assuming a mean initial velocity between 300 and 500 km/s is able to roughly reproduce the blue-shifted absorption profiles seen in the observation, while the model with 700 km/s produces absorption that is stronger than the observed one at velocities  $< -500$  km/s. The modeled down-the-barrel absorption profile is asymmetric, consistent with the observation. This is due to two effects of the hot gas: (1) the hot gas evaporates a fraction of outflow clouds as they move out, and (2) the ram pressure decelerates the clouds even when they are falling back towards the center.

Another observable that can be used to test the model prediction is the line of sight gas velocity dispersion. To derive such quantities with our models, we first estimate the gas covering fraction as a function of velocity and obtain mock absorption spectra as a function of impact parameters. To compare and mimic the observation from SDSS (Lan & Mo 2018), we first smooth the

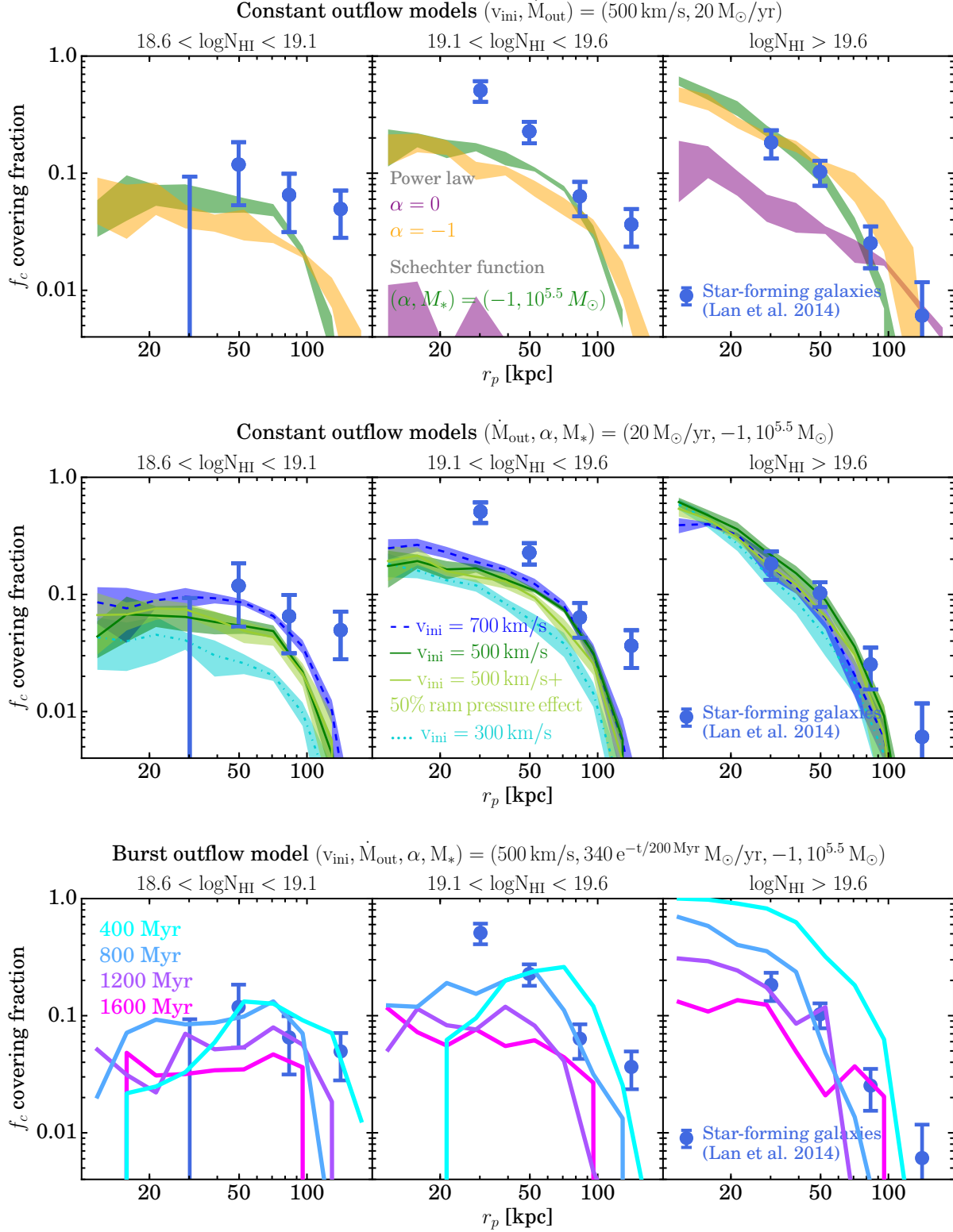


**Figure 8.** Covering fraction of gas clouds as a function of neutral hydrogen column density. The blue data points show the observed covering fraction from Lan et al. (2014). *Top:* Covering fraction as a function of initial cloud mass function. The results of power law mass functions with  $\alpha = 0$  and  $\alpha = -1$  are shown by purple and orange lines respectively. The green lines show the results from a Schechter like mass function with  $\alpha = -1$  and  $M_* = 10^{5.5} M_{\odot}$ . *Middle:* Covering fraction as a function of mean initial cloud velocity with 300, 500, and 700 km/s shown by dotted, solid, and dashed lines, respectively. *Bottom:* Covering fraction as a function of time with a burst outflow model.

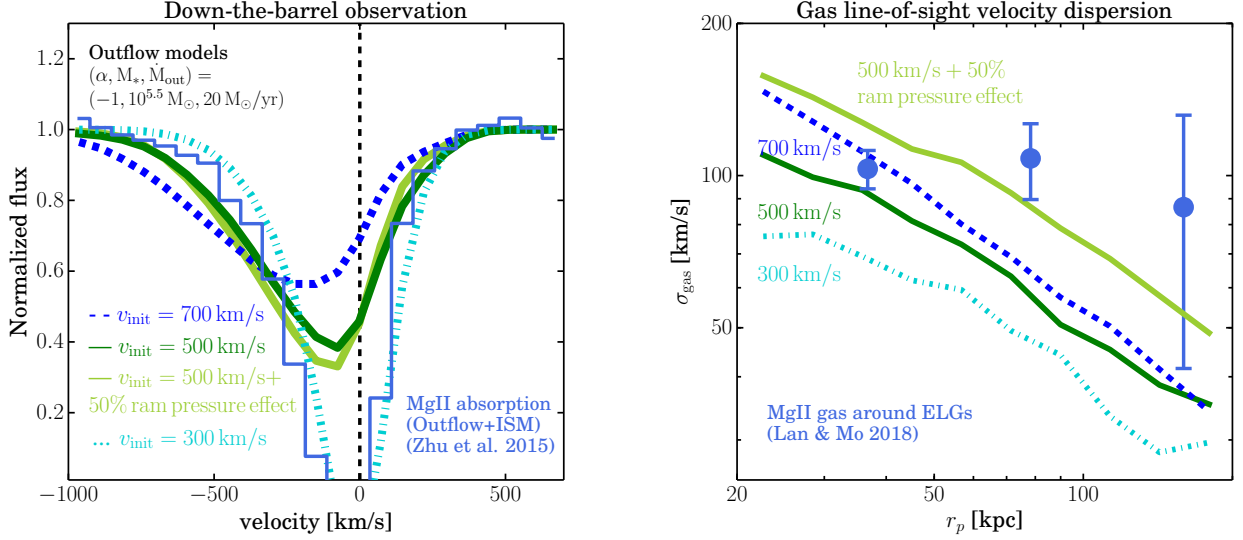


**Figure 9.** *Left:* Down-the-barrel blue-shifted outflow absorption. The blue histogram shows the observed down-the-barrel MgII absorption from Zhu et al. (2015) with emission-line filling corrected. *Right:* The line-of-sight velocity dispersion. The observed line-of-sight velocity dispersion of MgII gas from Lan & Mo (2018) is shown by the blue data points. In both panels, the lines show the modeled properties with initial velocity 300 (cyan dotted), 500 (green solid), and 700 (blue dashed) km/s. The light green line shows the model with initial velocity 500 km/s and 50% of the ram pressure efficiency.

mock absorption spectra with a Gaussian kernel with 70 km/s (SDSS spectral resolution) and then estimate the gas velocity dispersion by fitting the smoothed mock absorption spectra with a Gaussian profile. Finally, we subtract the spectral resolution in quadrature as done in Lan & Mo (2018). The right panel of Figure 9 shows the modeled line-of-sight velocity dispersion of pressure-confined outflow gas clouds. As expected, the gas velocity dispersion increases with the mean initial outflow velocity. The modeled gas velocity dispersion decreases with impact parameter due to the fact that the velocities of clouds are decelerated by both the gravity and the ram pressure of the hot gas. For clouds with  $M_{\text{cloud}} \sim 10^4 - 10^5 M_{\odot}$  that can reach large distances ( $\sim 100$  kpc, as shown in Figure 3), their velocities are only tens of km/s. This is in contrast to the observed gas line of sight velocity dispersion obtained from MgII absorption lines detected in the stacked background quasar spectra around star-forming galaxies, shown by the blue data points (Lan & Mo 2018). This indicates that some other mechanisms are needed to increase the gas velocity dispersion in the halos. One possible way is to reduce the deceleration from the ram pressure effect, as discussed below.

**The effects of ram pressure** - To explore how the ram pressure affect the properties of the gas, we adjust the ram pressure efficiency  $C_d$  in Equation 4 to be only 50% of the default value. The results are shown by the light green color in Figure 9. As one can see, lowering the ram pressure efficiency does not affect significantly the down-the-barrel absorption. This is because the absorption is mostly produced by gas clouds that have just

been ejected from the center (left panel of Figure 9). On the other hand, by lowering the ram pressure efficiency, the gas line-of-sight velocity dispersion is enhanced by about a factor of 1.5, closer to the observed values, as shown in the right panel of Figure 9. Lowering the ram pressure efficiency allows more gas clouds to travel to larger distances, but it does not affect the gas covering fraction significantly, as shown in the middle panel of Figure 8, where the gas covering fractions obtained from the default ram pressure efficiency and from 50% efficiency are shown by the green and light green lines, respectively.

These results indicate that only with a certain combination of parameters, the semi-analytic model considered here is able to reproduce the observed spatial distribution, down-the-barrel profile, and gas kinematics of cool CGM around star-forming galaxies. In other words, these observed gas properties together can provide strong constraints on physical models of outflows.

### 3.3.2. Burst outflow models

In addition to the constant outflow models, we show the covering fraction of gas predicted by the burst outflow model in the bottom panel of Figure 8. As shown in Figure 5, such models eject a large amount of mass into the CGM within  $\sim 300 - 400$  Myr, and in 1-2 Gyr the total mass decreases by more than 50% due to heat evaporation or gas recycling. The color lines show the evolution of covering fraction as a function of time. As can be seen, the covering fraction in the inner region decreases from 100% to 10% over the period from 400 Myr to 1600 Myr. This demonstrates that to maintain the

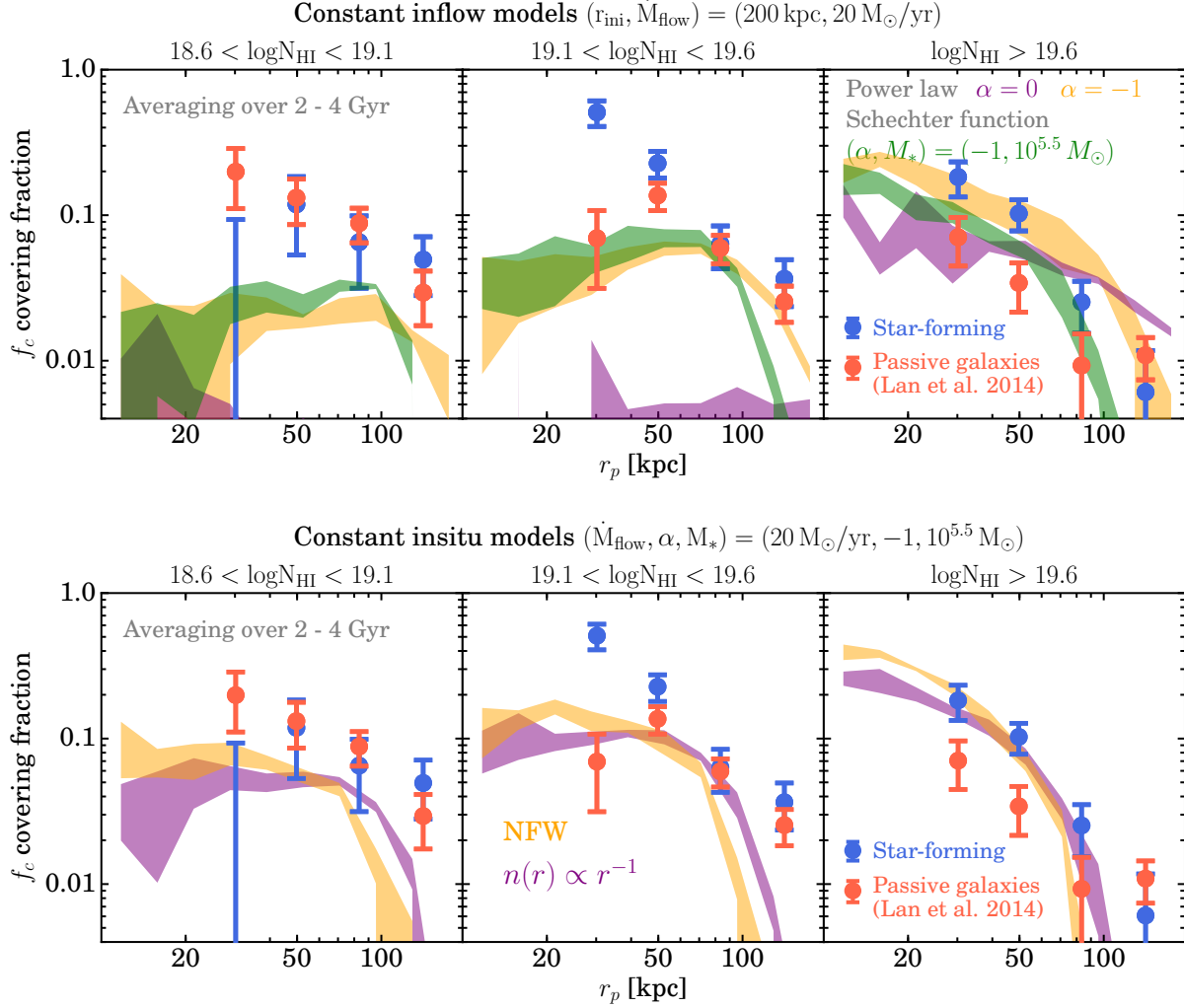


**Figure 10.** *Top:* Predicted covering fractions by inflow models as functions of the initial mass function. The results of power law mass functions with  $\alpha = 0$  and  $\alpha = -1$  are shown by purple and orange lines, respectively. The green lines show the results of a Schechter like mass function with  $\alpha = -1$  and  $M_* = 10^{5.5} M_\odot$ . *Bottom:* Predicted covering fractions by in-situ models with a NFW density profile (orange) and a power law profile (purple). The data points are covering fractions obtained by Lan et al. (2014).

amount of mass in the CGM over a long period time, a replenishment of the circumgalactic gas is required.

### 3.3.3. Inflow models

We now investigate the spatial distribution of gas clouds from the inflow models. Expected to occur around both star-forming and passive galaxies, gas inflows are a possible source of the cool gas observed around passive galaxies. In the following, we explore such a scenario by modeling the spatial distribution of cool gas clouds falling from the outskirts of the halos and compare the output with observations. The model assumes that gas clouds are initially located at 200 kpc from the halo center and fall towards the center of the halo with a constant mass flow rate of  $20 M_\odot/\text{yr}$ . The system is evolved over 4 Gyr. As shown in Figure 6, the

amount of mass in the CGM becomes stable after about 2 Gyr. The upper panel of Figure 10 shows the average covering fraction of the inflow gas clouds over a period from 2000 Myr to 4000 Myr for sightlines of different  $N_{\text{HI}}$ . Results are shown for different cloud mass functions: power laws with  $\alpha = 0$  and  $-1$  in purple and orange, respectively, and a Schechter function in green. The red and blue data points show the observed covering fraction based on MgII absorbers around passive and star-forming galaxies from Lan et al. (2014).

As in the outflow models, the covering fraction of the inflowing gas as a function of the HI column density depends on the shape of the initial mass function. The power law model with  $\alpha = 0$  (purple) produces only massive clouds, while steeper initial mass functions ( $\alpha = -1$ , orange, and a Schechter like, green) can pro-

duce more small clouds and therefore larger gas covering fractions that match better the observed ones.

Let us have a close look at the dependence of the shape of the covering fraction on  $N_{\text{HI}}$  predicted by the Schechter model of initial cloud mass function (green lines). The covering fraction of  $N_{\text{HI}} > 10^{19.6} \text{ cm}^{-2}$  (right panel) increases monotonically towards the center, while the covering fraction of  $N_{\text{HI}} < 10^{19.6} \text{ cm}^{-2}$  (left and middle panels) becomes flat or even decreases slightly towards the center. This difference is due to projection effect. The monotonic increasing trend of covering fraction for  $N_{\text{HI}} > 10^{19.6} \text{ cm}^{-2}$  is produced by relatively massive clouds that can survive long time and reach to the inner region of the halo where the clouds have higher  $N_{\text{HI}}$ , as shown in Figure 2. In contrast, due to the evaporation, there is no small clouds that can survive long enough to reach to the center and contribute to the covering fraction of  $N_{\text{HI}} < 10^{19.6} \text{ cm}^{-2}$ . Thus, the covering fraction of  $N_{\text{HI}} < 10^{19.6} \text{ cm}^{-2}$  within  $r_p < 100$  kpc is due to clouds at large distances  $> 100$  kpc but projected in the plane perpendicular to the line of sight. The projection yields to a flat covering fraction in the inner region. We note that for all the cases we have explored, the modeled covering fraction for clouds with  $10^{18.6} < N_{\text{HI}} < 10^{19.1} \text{ cm}^{-2}$  is always lower than the observed ones as shown in Figure 10. This is due to the fact that, with a given mass, only within a narrow range of locations beyond 100 kpc that clouds can have  $10^{18.6} < N_{\text{HI}} < 10^{19.1} \text{ cm}^{-2}$ , as shown in Figure 2. These results show that the inflow model can reproduce the observed covering fractions of high  $N_{\text{HI}}$  systems around passive galaxies within 100 kpc, but it fails to reproduce the low  $N_{\text{HI}}$  systems.

### 3.3.4. In-situ models

Gas clouds that form in-situ in the halos due to thermal instability and cooling (e.g., Kaufmann et al. 2006; Hummels et al. 2018) are another possible source for the cool gas observed around passive galaxies. We now consider and model this scenario by populating clouds falling in the halos with initial positions following a NFW and a power law,  $n(r) \propto r^{-1}$ , density distributions. The cloud mass formation rate is  $20 M_{\odot}/\text{yr}$  with the Schechter function of  $\alpha = -1$  and  $M_* = 10^{5.5} M_{\odot}$ . The covering fraction of clouds from the NFW profile (orange) and the power law (purple) are shown in the lower panel of Figure 10.

The surface mass density profile corresponding to a NFW profile is about  $\Sigma \propto r_p^{-1}$ , similar to the profile of the observed covering fraction. However, with a given cloud mass, the corresponding  $N_{\text{HI}}$  decreases with  $r_p$  because of the hot gas profile shown in Figure 2. These two factors together produce a sharp decrease of the covering fraction beyond 100 kpc.

In comparison to the NFW profile, the power law distribution produces a constant surface density profile, with more mass located in the outskirts. Consequently,

the profile of the covering fraction is more extended, as shown in the lower panel of Figure 10. However, the covering fraction in the inner region is lower than that predicted by the NFW profile. The inner profile of the covering fraction is also flatter due to the fact that the covering fraction is mostly contributed by clouds at larger distance in three-dimensional space. The power law distribution predicts covering fractions that are similar to the inflow models, but with an enhancement of covering fraction for high  $N_{\text{HI}}$  systems by a factor of  $\sim 1.5 - 2$  in the inner region due to clouds directly formed in-situ close to the center.

Comparing with the observed covering fractions, we conclude that both the gas clouds falling from the outskirts of the halo and clouds directly formed in-situ are able to explain the observed high  $N_{\text{HI}}$  systems around passive galaxies, but both fail to explain the low  $N_{\text{HI}}$  systems.

## 4. DISCUSSION

### 4.1. Dependence on other model parameters

Here we discuss how the properties of the cool gas depend on other parameters in the model.

#### 4.1.1. Dependence on hot gas

The properties of the cool clouds are affected by the adopted model for hot gaseous halos. Since the hot gas properties correlate with the halo masses in our model, we illustrate such an effect by calculating the properties of the cool gas as a function of halo mass while keep other parameters intact. Figure 11 shows the dependence of the hydrogen volume density and the neutral hydrogen column density on the halo mass. For the hot gas model adopted here, the pressure of hot gas at a given radius scale with the halo mass as  $M_{\text{halo}}^2$ , as reflected in the volume density of the cool gas shown in the upper panel. The lower panel shows the neutral hydrogen column density of clouds with a fixed cloud mass  $10^4 M_{\odot}$  as a function of halo mass indicated by the color lines. We find that clouds with  $N_{\text{HI}} > 10^{19} \text{ cm}^{-2}$  can only be found around halos with masses greater than  $\sim 10^{11.75} M_{\odot}$  due to the fact that hydrogen in cool clouds becomes highly ionized when the volume density is low.

This result suggests that absorbers with high column density in neutral hydrogen e.g.  $N_{\text{HI}} > 10^{19} \text{ cm}^{-2}$  and single-ionized gas (e.g., MgII, SiII) only exist in halos that can provide sufficient pressure-support from hot ambient gas. In addition, the high column density systems are preferentially found near the center of the halos where the pressure of the hot gas is expected to be higher. Thus, this model of pressure-confined gas cloud predicts that the incidence rate of absorbers with high column density in neutral hydrogen and in single-ionized metal elements increases with halo mass while decreases with radius. This trend is consistent with observations that high neutral hydrogen column density



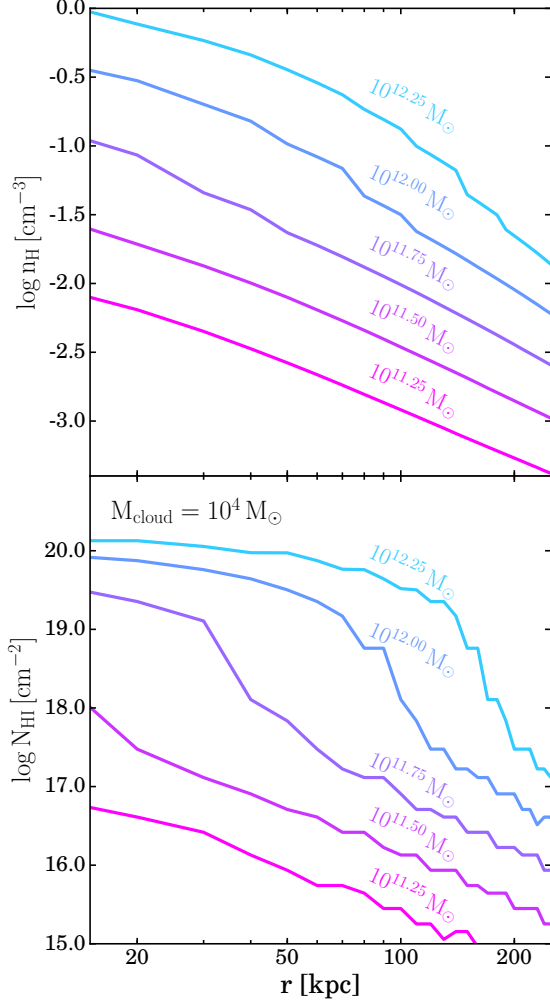


**Figure 11.** Hydrogen volume density and neutral hydrogen column density as a function of halo mass and position. *Top:* Hydrogen volume density. *Bottom:* Neutral hydrogen column density for clouds with  $10^4 M_\odot$ .

systems, such as strong MgII absorbers, sub-DLAs and DLAs, tend to be found around massive galaxies (e.g., Chen et al. 2010; Lan et al. 2014; Kanekar et al. 2018).

#### 4.1.2. Evaporation factor

In Equation (8), we introduce a factor  $f$  to control the efficiency of cloud mass loss due to evaporation. This factor affects the amount of mass in the circumgalactic medium by reducing the lifetime of clouds. In our model, we set  $f$  to be 5%. If  $f$  is taken to be 100%, i.e. 20 times as high as we adopt, the gas flow rate needs to be increased by a factor of 20 in order to maintain the same amount of the mass in the CGM. This leads to an unreasonably high value of the gas flow rate, about  $400 M_\odot/\text{yr}$  for the constant outflow/inflow models to match the observed covering fractions. In addition, high

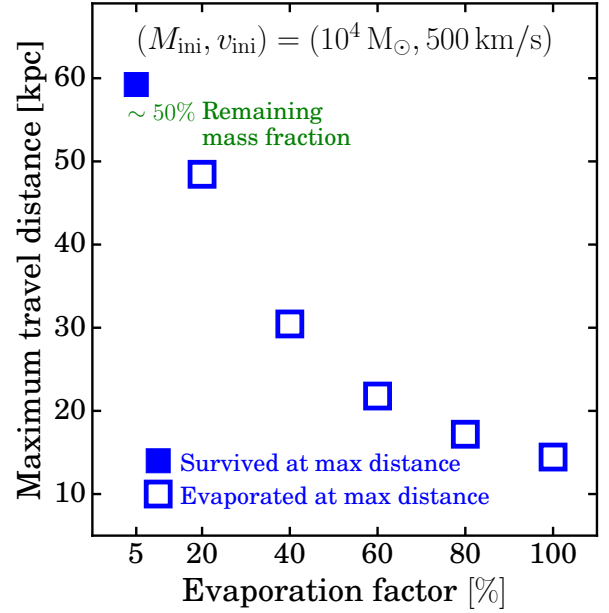


**Figure 12.** The effect of the evaporation factor on the maximum travel distance of clouds. With 5% efficiency, clouds with 500 km/s and  $10^4 M_\odot$  can reach 60 kpc with  $\sim 50\%$  of initial mass, while with 100% efficiency, the clouds lose all the mass at 15 kpc.

$f$  will reduce the travel distances of outflow clouds and, therefore, the extension of the cool circumgalactic clouds originated from galaxies.

In Figure 12, we show the effect of the evaporation efficiency on the travel distance of gas clouds ejected from the center with 500 km/s initial velocity and  $10^4 M_\odot$  initial cloud mass. The figure shows that with the evaporation factor we adopt, 5%, the gas cloud can travel to about 60 kpc from the center while retain about 50% of the initial mass at the maximum distance determined by gravity and the ram pressure of the system. In contrast, for higher evaporation factors, gas clouds lose all the mass while moving outwards and the maximum distances are set by the evaporation. With 100% evaporation factor, the maximum travel distance is only 15 kpc. This result illustrates that low evaporation factor is needed to produce the cool CGM with reasonable parameter values.

#### 4.2. The evaporated gas in the CGM

Our model shows that a significant fraction ( $\sim 50\%$  for  $\alpha = -1$  and  $\sim 80\%$  for a Schechter mass function) of total ejected cloud mass is evaporated. This suggests that the circumgalactic medium also contains the evaporated gas. Although the physics of the evaporated gas is not well-developed and not included in our model, the temperature and the density of the evaporated gas are

expected to be between that of pressure-confined gas clouds and that of the hot ambient gas over a certain timescale (e.g., Balbus & Potter 2016). This may be investigated with high resolution hydrodynamic simulations for individual clouds (e.g., Armillotta et al. 2017; Liang & Remming 2018; Sparre et al. 2018). For example, Armillotta et al. (2017) demonstrate that the interaction between the hot ambient gas and the pressure-confined clouds can produce evaporated and stripped gas with relatively low column density, and highly ionized species, such as SiIII and OVI (their Figure 3 and Figure 6). These results demonstrate that the evaporated gas may be responsible for a significant fraction of the relatively highly-ionized absorption line systems, such as CIV and OVI, and perhaps some low column density systems of lowly-ionized species, such as MgII. It is important to understand the properties of such gas in detail in order to have a complete picture of the CGM.

#### 4.3. Comparisons with other studies

**A universal density model** - Motivated by observations, Stern et al. (2016) develop a hierarchical density structure model for the circumgalactic medium assuming that the density structure of the circumgalactic medium follows a power law distribution with high density gas embedded in the low density one. They show that this density structure can simultaneously reproduce the column densities of metal species in neutral (e.g., MgI) to highly ionized phase (e.g., OVI) at redshift 0.1. Despite that this model and our model start with different assumptions, the two predict similar MgII gas properties: cloud sizes about 50 pc and cloud masses about  $10^2 - 10^3 M_\odot$  (See their Table 1).

**Shattering cloudlet model** - Recently, McCourt et al. (2018) propose that the pressure-confined cool gas clouds will be fragmented into tiny droplets with a characteristic scale with  $N_{\text{H}} \sim 10^{17} \text{cm}^{-2}$  corresponding to the scale of the product of sound velocity and cooling time. This property has been demonstrated in high-resolution hydrodynamical simulations (e.g., McCourt et al. 2018; Liang & Remming 2018; Sparre et al. 2018). As discussed in McCourt et al. (2018), for a single droplet with  $N_{\text{H}} \sim 10^{17} \text{cm}^{-2}$ , the gas is optical thin and highly ionized; However, a collection of droplets can be self-shielded and produce systems with high neutral hydrogen column densities. In some sense, a single cloud in our model can be considered as a collection of droplets which are physically associated with each other and move together.

**Cool gas inconsistent with the pressure equilibrium scenario** - Using the data from COS on the Hubble telescope, Werk et al. (2014) characterized the physical properties of the gas around galaxies at redshift  $\sim 0.1$ . Using the CLOUDY simulation, they found that the detected cool gas has volume density to be  $10^{-3} - 10^{-4} \text{cm}^{-3}$ , inconsistent with the density of pressure-confined cool gas in  $10^{12} M_\odot$  halos. They concluded

that the scenario in which cool circumgalactic gas is in the pressure equilibrium is a poor description of the CGM. However, as shown in this study, the gas clouds in pressure equilibrium are expected to be most neutral with high neutral hydrogen column densities  $N_{\text{H}} > 10^{18.5} \text{cm}^{-2}$ , and with the covering fraction traced by strong MgII absorbers at most 20 – 30% at 50 kpc and 5 – 10% at 100 kpc. Having 44 sightlines intercepting the CGM of galaxies with a wide range of halo masses from  $10^{11.3}$  to  $10^{13.5} M_\odot$  (Tumlinson et al. 2013), it is possible that the pressure-confined gas clouds are not well sampled by the observation and most of the sightlines intercept some diffuse gas, such as evaporated gas in our model, which may have a range of temperatures and may not be in pressure equilibrium with the hot gas. In addition, it is possible that a single phase model is not adequate to capture the underlying multiphase gas structure as illustrated in Stern et al. (2016). Given above, we argue that more data and advanced modeling are required to better test the scenario of the pressure equilibrium.

#### 4.4. Limitations and directions for future work

**Hot gas** - As shown in this work, the pressure confined cool gas properties depend on the assumed hot gas properties. In our model, we assume that the hot gas is in hydrostatic equilibrium. However, it may not reflect the real properties of hot gas as suggested by Oppenheimer (2018). In addition, we only consider the hot gas profile from a halo with  $10^{12} M_\odot$  when comparing with observations. However, the observed covering fractions are expected to be obtained from a galaxy population living in halos with a range of mass. For future studies, one needs to take this halo mass dependence into account.

**Cool gas** - we calculate the physical properties of the cool gas by assuming that the cloud temperature is a constant  $10^4 \text{K}$ . However, it is expected that the cloud temperature can vary depending on the heating mechanisms. We have performed a calculation by adjusting the cloud temperature. If the cloud temperature is assumed to be 5000 K, the column density,  $N_{\text{H}}$ , will be enhanced for a given cloud mass. Therefore, for the initial mass function with  $\alpha = -1$  and  $M^* = 10^{5.5} M_\odot$  adopted in this work, the model will produce more  $N_{\text{H}} > 10^{19.5} \text{cm}^{-2}$  systems and overproduce the gas covering fraction for such systems. On the other hand, by increasing the temperature of clouds to be 20000 K, all the gas clouds become highly ionized with  $N_{\text{H}} < 10^{19} \text{cm}^{-2}$ . Such a scenario cannot produce any high column density systems as observed. This suggests that the adopted cloud temperature with  $10^4 \text{K}$  is perhaps reasonable for reproducing the gas properties of high  $N_{\text{H}}$  gas absorbers.

**Survival of clouds** - One of the key assumptions in our model is that the clouds are not destroyed by the hydrodynamic instability. Although a number of stud-

ies have shown that various mechanisms can suppress the effect of hydrodynamical instability (e.g., Vietri et al. 1997; McCourt et al. 2015; Armillotta et al. 2017; Gronke & Oh 2018), it is still unclear how these mechanisms operate in reality. This problem is related to the problem of entraining the cool gas along with a hot wind (e.g., Zhang et al. 2017). However, we argue that the existence of cool gas and the evidence of contribution from outflows in the halos (e.g., Bordoloi et al. 2011; Lan & Mo 2018) suggest that either the cool gas outflows must survive over the hydrodynamic instability, as we assume in our model, or cool gas is redistributed in the halos by some other mechanisms associated with outflows (e.g., Thompson et al. 2016; Lochhaas et al. 2018).

**Gas properties at large scales** - Our model has difficulties in explaining systems with  $N_{\text{HI}} > 10^{19} \text{ cm}^{-2}$  beyond 100 kpc (e.g., Zhu et al. 2014; Huang et al. 2016; Lan & Mo 2018) due to the low volume density of the hot ambient gas as shown in Figure 2. It is, therefore, likely that some of the systems at large distances are produced by neighboring halos due to spatial clustering of halos. Such ‘two-halo’ term is not included in our current model, but should be modeled.

## 5. SUMMARY

We develop a flexible semi-analytic framework to explore the physical properties of the cool pressure-confined circumgalactic clouds with mass from  $10 M_{\odot}$  to  $10^8 M_{\odot}$ . We take into account the effects of gravity and interaction between hot gas and cool gas and model the trajectory, the lifetime, and the observed properties of the cool clouds with CLOUDY simulations. The ensemble properties of the cool CGM are explored by populating clouds following various mass functions in the halos with three origins, outflows, inflows, and in-situ formation. With this framework, we investigate how different mechanisms affect the observed properties of the cool CGM. Our results are summarized as follows:

1. The pressure-confined cool gas clouds have  $N_{\text{HI}} > 10^{18.5} \text{ cm}^{-2}$  with sizes about 10-100 pc similar to the observed properties of strong metal absorbers, sub-DLAs, and DLAs observed towards background spectra.
2. We illustrate the effect of hot gas on the motion and lifetime of cool gas clouds; the ram pressure from the hot gas prevents most of the high velocity cool clouds from escaping the system and heat evaporation destroys small clouds in about hundred million years. Because of these mechanisms and gas recycling, the cool CGM is transient and therefore a constant replenishment is required to sustain it.
3. We demonstrate that the morphology and structure of the CGM depend on the shape of the initial

cloud mass function. A Schechter-like mass function is favored in order to produce covering fractions as a function of HI column density that are comparable to the observed ones.

4. We show that only with certain combinations of parameters can the model reproduce the three gas properties of star-forming galaxies: the spatial distribution, down-the-barrel outflow absorption, and gas velocity dispersion at the same time. This demonstrates the constraining power of the observed CGM properties on physical models of outflows.
5. We show that high  $N_{\text{HI}}$  gas around passive galaxies may also be explained by in-situ gas clouds and gas inflow, while such models under-produce low  $N_{\text{HI}}$  systems.
6. We demonstrate how the cool gas properties depend on the assumed halo mass and evaporation efficiency. This model predicts that high neutral hydrogen column density systems should tend to be found in massive halos and close to the center where the hot gas pressure is expected to be the highest. In addition, to maintain the cool CGM with a more realistic gas flow rate, the heat evaporation factor needs to be much lower than the classical efficiency.

These results demonstrate that analytic and semi-analytic approaches are another promising way to understand and explore physical mechanisms that govern the properties of the cool CGM without limited by the numerical resolution as indicated by recent simulations and theoretical models (e.g., McCourt et al. 2018; Sparre et al. 2018; van de Voort et al. 2018; Peebles et al. 2018; Hummels et al. 2018). Finally, we list two key properties of the pressure-confined cool CGM which can be tested by future observations:

- The pressure of hot gas halo increases with halo mass and decreases with impact parameter. These dependences are expected to be reflected in the properties of the pressure-confined cool CGM. With a statistical sample, one can possibly map out the pressure profile of cool gas as a function of halo mass and impact parameter and confront the observation with this model (e.g. Werk et al. 2014; Zahedy et al. 2018).
- Based on the blueshifted absorption line profile observed down-the-barrel, the typical velocity of cool gas outflows is about a few hundred km/s. Our model shows that most of cool gas clouds with such initial velocities can not escape the halos. They are mostly confined within 100 kpc (Figure 3). Therefore, the gas clouds are expected to enhance the covering fraction and metallicity within

such a scale. This scenario can be tested by probing the covering fraction (e.g. [Lan & Mo 2018](#)) and metallicity profiles (e.g. [Péroux et al. 2016](#)) of cool gas around star-forming galaxies as a function of impact parameters.

We thank J. Xavier Prochaska, Neal Katz, and Brice Ménard for insightful discussions. We also want to

thank the anonymous referee for the constructive report. HJM acknowledges support from NSF AST-1517528, and from National Science Foundation of China (grant Nos. 11673015, 11733004). Kavli IPMU is supported by World Premier International Research Center Initiative of the Ministry of Education, Japan.

## REFERENCES

- Anglés-Alcázar, D., Faucher-Giguère, C.-A., Kereš, D., et al. 2017, *MNRAS*, 470, 4698
- Armillotta, L., Fraternali, F., Werk, J. K., Prochaska, J. X., & Marinacci, F. 2017, *MNRAS*, 470, 114
- Balbus, S. A., & Potter, W. J. 2016, *Reports on Progress in Physics*, 79, 066901
- Bergeron, J. 1986, *A&A*, 155, L8
- Binney, J., & Cowie, L. L. 1981, *ApJ*, 247, 464
- Bordoloi, R., Lilly, S. J., Knobel, C., et al. 2011, *ApJ*, 743, 10
- Bordoloi, R., Lilly, S. J., Kacprzak, G. G., & Churchill, C. W. 2014, *ApJ*, 784, 108
- Bordoloi, R., Wagner, A. Y., Heckman, T. M., & Norman, C. A. 2017, *ApJ*, 848, 122
- Bruzual, G., & Charlot, S. 2003, *MNRAS*, 344, 1000
- Chandran, B. D. G., & Cowley, S. C. 1998, *Physical Review Letters*, 80, 3077
- Chen, H.-W., Helsby, J. E., Gauthier, J.-R., et al. 2010, *ApJ*, 714, 1521
- Cowie, L. L., & McKee, C. F. 1977, *ApJ*, 211, 135
- Dalton, W. W., & Balbus, S. A. 1993, *ApJ*, 404, 625
- Faucher-Giguère, C.-A., Feldmann, R., Quataert, E., et al. 2016, *MNRAS*, 461, L32
- Faerman, Y., Sternberg, A., & McKee, C. F. 2017, *ApJ*, 835, 52
- Ferland, G. J., Porter, R. L., van Hoof, P. A. M., et al. 2013, *RMXAA*, 49, 137
- Ford, A. B., Davé, R., Oppenheimer, B. D., et al. 2014, *MNRAS*, 444, 1260
- Gupta, A., Mathur, S., & Krongold, Y. 2017, *ApJ*, 836, 243
- Gronke, M., & Oh, S. P. 2018, *arXiv:1806.02728*
- Haardt, F., & Madau, P. 2001, *Clusters of Galaxies and the High Redshift Universe Observed in X-rays*, 64
- Huang, Y.-H., Chen, H.-W., Johnson, S. D., & Weiner, B. J. 2016, *MNRAS*, 455, 1713
- Hummels, C. B., Smith, B. D., Hopkins, P. F., et al. 2018, *arXiv e-prints*, *arXiv:1811.12410*.
- Jeans, J. H. 1902, *Philosophical Transactions of the Royal Society of London Series A*, 199, 1
- Jones, T., Stark, D. P., & Ellis, R. S. 2018, *ApJ*, 863, 191
- Kacprzak, G. G., Churchill, C. W., & Nielsen, N. M. 2012, *ApJL*, 760, L7
- Kaufmann, T., Mayer, L., Wadsley, J., Stadel, J., & Moore, B. 2006, *MNRAS*, 370, 1612
- Kaufmann, T., Bullock, J. S., Maller, A. H., Fang, T., & Wadsley, J. 2009, *MNRAS*, 396, 191
- Kanekar, N., Prochaska, J. X., Christensen, L., et al. 2018, *ApJL*, 856, L23
- Lan, T.-W., Ménard, B., & Zhu, G. 2014, *ApJ*, 795, 31
- Lan, T.-W., & Fukugita, M. 2017, *ApJ*, 850, 156
- Lan, T.-W., & Mo, H. 2018, *ApJ*, 866, 36
- Liang, C. J., & Remming, I. S. 2018, *arXiv:1806.10688*
- Lochhaas, C., Thompson, T. A., Quataert, E., & Weinberg, D. H. 2018, *MNRAS*, 481, 1873
- Maller, A. H., & Bullock, J. S. 2004, *MNRAS*, 355, 694
- Mathews, W. G., & Prochaska, J. X. 2017, *ApJL*, 846, L24
- Ménard, B., & Chelouche, D. 2009, *MNRAS*, 393, 808
- McCourt, M., O’Leary, R. M., Madigan, A.-M., & Quataert, E. 2015, *MNRAS*, 449, 2
- McCourt, M., Oh, S. P., O’Leary, R., & Madigan, A.-M. 2018, *MNRAS*, 473, 5407
- McQuinn, M., & Werk, J. K. 2018, *ApJ*, 852, 33
- Mo, H. J., & Miralda-Escude, J. 1996, *ApJ*, 469, 589
- Peeples, M. S., Corlies, L., Tumlinson, J., et al. 2018, *arXiv:1810.06566*
- Murray, S. D., White, S. D. M., Blondin, J. M., & Lin, D. N. C. 1993, *ApJ*, 407, 588
- Murray, N., Ménard, B., & Thompson, T. A. 2011, *ApJ*, 735, 66
- Navarro, J. F., Frenk, C. S., & White, S. D. M. 1996, *ApJ*, 462, 563
- Nelson, D., Kauffmann, G., Pillepich, A., et al. 2018, *MNRAS*, 477, 450
- Nielsen, N. M., Churchill, C. W., & Kacprzak, G. G. 2013, *ApJ*, 776, 115
- Nipoti, C., & Binney, J. 2004, *MNRAS*, 349, 1509
- Oppenheimer, B. D. 2018, *MNRAS*, 480, 2963

- Péroux, C., Quiret, S., Rahmani, H., et al. 2016, MNRAS, 457, 903
- Prochaska, J. X., & Hennawi, J. F. 2009, ApJ, 690, 1558
- Rauch, M., Sargent, W. L. W., & Barlow, T. A. 1999, ApJ, 515, 500
- Rao, S. M., Turnshek, D. A., & Nestor, D. B. 2006, ApJ, 636, 610
- Rigby, J. R., Charlton, J. C., & Churchill, C. W. 2002, ApJ, 565, 743
- Rubin, K. H. R., Prochaska, J. X., Koo, D. C., et al. 2014, ApJ, 794, 156
- Sparre, M., Pfrommer, C., & Vogelsberger, M. 2018, arXiv:1807.07971
- Stern, J., Hennawi, J. F., Prochaska, J. X., & Werk, J. K. 2016, ApJ, 830, 87
- Stern, J., Faucher-Giguère, C.-A., Hennawi, J. F., et al. 2018, arXiv:1803.05446
- Suresh, J., Nelson, D., Genel, S., Rubin, K. H. R., & Hernquist, L. 2018, MNRAS,
- Thompson, T. A., Quataert, E., Zhang, D., & Weinberg, D. H. 2016, MNRAS, 455, 1830
- Tumlinson, J., Thom, C., Werk, J. K., et al. 2011, Science, 334, 948
- Tumlinson, J., Thom, C., Werk, J. K., et al. 2013, ApJ, 777, 59
- Tumlinson, J., Peeples, M. S., & Werk, J. K. 2017, ARA&A, 55, 389
- Thom, C., Tumlinson, J., Werk, J. K., et al. 2012, ApJL, 758, L41
- van de Voort, F., Springel, V., Mandelker, N., van den Bosch, F. C., & Pakmor, R. 2018, arXiv:1808.04369
- Vietri, M., Ferrara, A., & Miniati, F. 1997, ApJ, 483, 262
- Werk, J. K., Prochaska, J. X., Tumlinson, J., et al. 2014, ApJ, 792, 8
- Yang, X., Mo, H. J., van den Bosch, F. C., 2003, MNRAS, 339, 1057
- Yang, X., Mo, H. J., van den Bosch, F. C., Zhang, Y., Han, J. 2012, ApJ, 752, 41
- Zahedy, F. S., Chen, H.-W., Johnson, S. D., et al. 2018, arXiv:1809.05115
- Zhang, D., Thompson, T. A., Quataert, E., & Murray, N. 2017, MNRAS, 468, 4801
- Zhu, G., Ménard, B., Bizyaev, D., et al. 2014, MNRAS, 439, 3139
- Zhu, G. B., Comparat, J., Kneib, J.-P., et al. 2015, ApJ, 815, 48